Eur Radiol (2009) 19: 2739–2749
DOI 10.1007/s00330-009-1457-8

ULTRASOUND

Emily Y. Wong
Hristo N. Nikolov
Meghan L. Thorne
Tamie L. Poepping
Richard N. Rankin
David W. Holdsworth

Clinical Doppler ultrasound for the assessment of plaque ulceration in the stenosed carotid bifurcation by detection of distal turbulence intensity: a matched model study

Received: 22 October 2008
Revised: 2 April 2009
Accepted: 10 April 2009
Published online: 23 June 2009

E. Y. Wong · H. N. Nikolov · M. L. Thorne · D. W. Holdsworth (✉)
Robarts Research Institute
University of Western Ontario,
100 Perth Drive,
London, ON, Canada, N6A 5K8
e-mail: David.Holdsworth@imaging.robarts.ca
Tel.: +1-519-663-5777
Fax: +1-519-663-3900

E. Y. Wong · M. L. Thorne · T. L. Poepping · D. W. Holdsworth
Department of Medical Biophysics,
University of Western Ontario,
London, ON, Canada

T. L. Poepping
Department of Physics and Astronomy,
University of Western Ontario,
London, ON, Canada

R. N. Rankin
Department of Medical Imaging,
University of Western Ontario,
London, ON, Canada

D. W. Holdsworth
Department of Surgery,
University of Western Ontario,
London, ON, Canada

Abstract The assessment of flow disturbances due to carotid plaque ulceration may provide added diagnostic information to Doppler ultrasound (DUS) of the carotid stenosis, and indicate whether the associated hemodynamics are a potential thromboembolic source. We evaluated the effect of ulceration in a moderately stenosed carotid bifurcation on distal turbulence intensity (TI) measured using clinical DUS in matched anthropomorphic models. Several physiologically relevant ulcer geometries (hemispherical, mushroom-shaped, and ellipsoidal pointing distally and proximally) and sizes (2-mm, 3-mm and 4-mm diameter hemispheres) were investigated. An offline analysis was performed to determine several velocity-based parameters from ensemble-averaged spectral data, including TI. Significant elevations in TI were observed in the post-stenotic flow field of the stenosed carotid bifurcation by the inclusion of ulceration ($P<0.001$) in a region two common carotid artery diameters distal to the site of ulceration during the systolic peak and the diastolic phase of the cardiac cycle. Both the size and shape of ulceration had a significant effect on TI in the distal region ($P<0.001$). Due to the use of a clinical system, this method provides the means to evaluate for plaque ulcerations in patients with carotid atherosclerosis using DUS.

Keywords Doppler ultrasound · Plaque ulceration · Carotid artery · Turbulence intensity · Flow models

Introduction

Doppler ultrasound (DUS), utilizing peak-systolic velocity measurements within the high-velocity jet of the internal carotid artery (ICA) as a surrogate measure of stenosis severity, is commonly the first-line diagnostic technique used in the assessment of stroke patients [1]. However, atherosclerotic carotid vessels of similar stenosis or hemodynamic severity do not necessarily pose the same risk of thromboembolic events, and current examinations based solely on the evaluation of stenosis severity do not provide optimal sensitivity and specificity for the selection of patients appropriate for surgery [2, 3]. In addition to the degree of ICA stenosis, the North American Symptomatic Carotid Endarterectomy Trial (NASCET) identified one other angiographic parameter—the presence of carotid plaque ulceration—as an independent risk factor for stroke [4]. Even when the percent stenosis is less than severe (i.e. < 70% by NASCET standard), there is evidence that plaque surface ulceration can be a source of cerebral embolisms and a potential cause of thrombosis in the carotid artery [5, 6]. This clearly demonstrates the clinical impetus for a diagnostic

indicator of plaque ulceration, in addition to stenosis severity, as part of DUS examinations of carotid artery disease.

It is well established that the stenosed carotid bifurcation is uniquely susceptible to complex and aberrant flow behaviour [7]. Moreover, plaque surface roughness can further contribute to the abnormality of local hemodynamics, particularly to disturbed flow patterns downstream [8, 9]. Local alterations in blood-flow, such as vortices, disturbed flow, high or oscillating shear stress, and turbulence, have been demonstrated to promote thrombus formation [10–12]. Therefore, an assessment of the post-stenotic velocity field in ulcerated atherosclerotic vessels, using a method able to detect departures from laminar flow, may be of diagnostic utility. A post-stenotic evaluation may also ascertain whether fluid dynamic mechanisms of thrombogenesis contribute to the increased risk of ischemic events associated with ulcerated lesions.

In addition to the measurements of peak velocities used in current diagnostic examinations, DUS has the capability to observe quantitative and absolute measures of disturbed and turbulent physiological flow [13–15]. While there are several DUS spectral parameters that are indicative of disturbances in blood-flow, turbulence intensity (TI) is of particular interest, as it is a direct measure of velocity fluctuations and is subject to fewer confounding factors than indices based on spectral width and Doppler backscatter [16, 17].

We describe an in-vitro study of physiologically relevant ulceration in a stenosed anthropomorphic carotid flow phantom, using clinical DUS to characterize TI distal to the bifurcation. This method allows for the direct comparison of downstream flow with and without the presence of ulceration, in the same stenosis geometry and under identical physiological flow conditions. An offline analysis of data from the clinical system was used to calculate ensemble averaged velocity parameters and compare post-stenotic velocity data in the models. The effects of ulcer size and geometry on the resultant spectral parameters are presented.

Materials and methods

Phantom design

Vessel and ulcer geometry

A set of anthropomorphic DUS-compatible flow phantoms with ulcers of various sizes and geometries were constructed using the direct-fabrication technique described by Wong et al. [18] The underlying baseline vessel geometry of each phantom, before the incorporation of ulceration, was an averaged geometric representation of a human carotid bifurcation [19], with 50% eccentric stenosis under NASCET criteria [20] and a common carotid artery (CCA) diameter of 8 mm. Four ulcer shapes—representing each of the four clinically-determined categories defined by Lovett et al. [21] (as indicated in parentheses)—were investigated: a hemispherical ulceration (Type I), a mushroom-shaped ulcer incorporating a cavity with a small neck connecting it to the parent vessel lumen (Type II), and ellipsoidal ulcers pointing distally (Type III) and proximally (Type IV).

Three-dimensional (3D) computer-aided design (CAD) models representing the reported ulcer geometries were generated in a CAD software package (MasterCam, CNC Software, Tolland, Conn.) by constructively assembling geometric primitives. The vessel lumen was defined by the intersection of the geometric primitives with the parametrically defined baseline carotid bifurcation geometry. The dimensions of each ulcer type were designed to be clinically realistic in size, proportions, angle of incidence [9, 21–25], and to maintain a similar cavity volume between ulcers. Each ulcer was incorporated into a carotid vessel geometry at the level of the apex of the bifurcation on the non-flow divider wall, to be consistent with previous characterizations of frequent sites of carotid plaque ulceration [22, 24]. A Type I, 4-mm diameter hemispherical ulcer was achieved by incorporating a 4-mm diameter sphere centred at the vessel lumen surface. A Type II, mushroom-shaped ulcer was constructed as a prolate ellipsoid with an aspect ratio of 2.5 (major axis 5.36 mm, minor axis 2.14 mm) coupled with a cylindrical neck of diameter 2.14 mm and length of 1.07 mm from the main lumen-wall boundary to the ellipsoidal centre. Type III and IV ellipsoidal ulcers were modelled as prolate ellipsoids with an aspect ratio of 2.5 (major axis 7.37 mm, minor axis 2.95 mm) and with the centre intersecting the main lumen-wall boundary, tilted at 45° relative to the tangent of the lumen surface at the level of the bifurcation apex. To investigate the effect of ulcer size, two additional vessel geometries incorporating hemispherical ulcers (diameters of 2 and 3 mm) were manufactured. No ulcer was allowed to extend beyond the boundary defined by the corresponding averaged representation of a normal carotid bifurcation lumen geometry [19]. A non-ulcerated phantom with the baseline stenosis geometry was fabricated for comparison with the ulcerated models. The CAD geometries for each of the bifurcation phantoms are shown in Fig. 1.

Fabrication technique

The procedures for the milling and assembly of the phantoms are described in detail by Wong et al. [18] Dimensional accuracy and geometric fidelity of the flow phantoms were evaluated using high-resolution micro-computed tomography (micro-CT) (Locus Ultra, General Electric Healthcare Biosciences, London, Canada), as previously described [18]. Root-mean-squared (RMS) departures from prescribed CAD dimensions are reported.

Doppler data acquisition

Cardiac-gated Doppler flow velocity data were collected in each of the carotid bifurcation phantoms under identical

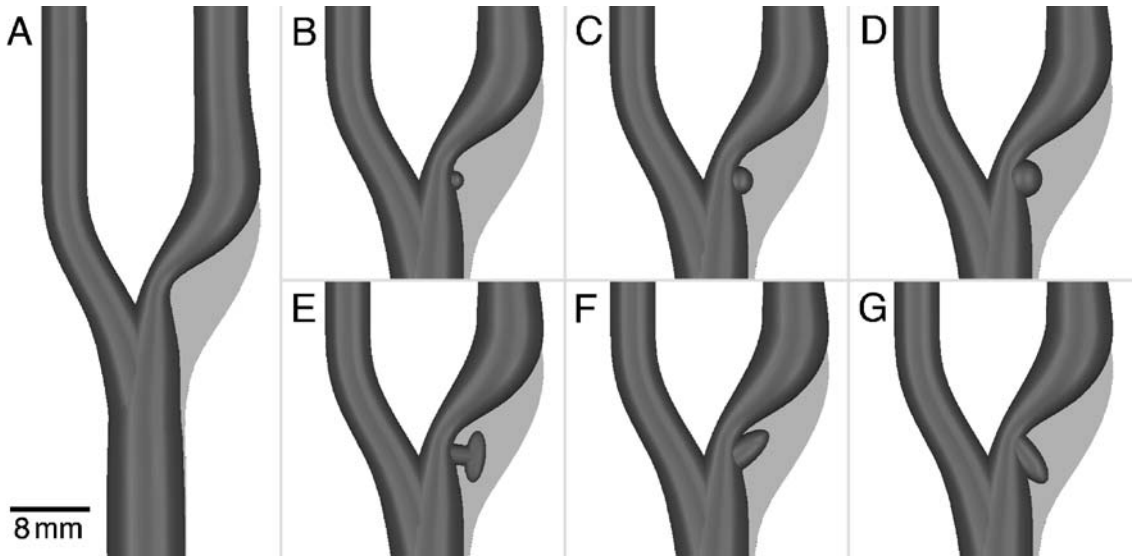

Fig. 1 The carotid bifurcation lumen geometries used in our study. The CAD models are of an idealized 50% eccentric carotid bifurcation with (**A**) a smooth non-ulcerated wall; a hemispherical ulcer of (**B**) 2-mm, (**C**) 3-mm and (**D**) 4-mm diameter; (**E**) a mushroom-shaped ulcer; an ellipsoidal ulcer pointing (**F**) distally and (**G**) proximally. The normal carotid bifurcation geometry is shown in *light grey* to illustrate the location of plaque deposition

Doppler acquisition parameters and physiological pulsatile flow conditions using an in-vitro flow simulator and semiautomated DUS acquisition system, as described by Poepping et al. [26] A well-characterized blood-mimicking fluid (BMF) suited to DUS blood-velocity measurements under both laminar and turbulent flow conditions was used [27, 28]. A simulated average carotid flow-rate waveform [29], with a mean flow rate of 6.00 ml·s^{-1}, a peak flow rate of 23.46 ml·s^{-1}, and a cycle length of 0.92 s, was provided to the CCA inlet of the flow phantom using a computer-controlled flow pump [30], resulting in a mean Reynolds number of 238 and a Womersley number of 5.2. In the stenosis (2.8-mm diameter), the mean and peak Reynolds numbers were 450 and 1,770, respectively. The flow phantoms were mounted in a water bath during ultrasound acquisition to ensure adequate acoustic coupling. Experiments were conducted at a temperature of 23±1°C.

Doppler spectral data were acquired at a clinical Doppler collection angle of 60° with a conventional clinical duplex DUS system (Ultramark 9, Philips-ATL, Bothell, Wash.) using a 4-MHz linear array transducer (L7–4, Philips-ATL, Bothell, Wash.) producing a focused beam with a 2.0-cm focal depth and a 1.0-mm sample volume length. A pulse-repetition frequency of 18,519 Hz was used to prevent aliasing of the Doppler signal in the high-velocity regions. The lowest available wall filter setting of 50 Hz was applied. A semiautomated acquisition system equipped with a computer-controlled 3D translating stage was used to collect DUS data over the central plane of the phantom defined by the longitudinal axes of the bifurcation flow phantom, as described by Poepping et al. [26] The acquisition grid consisted of 1,025 sample locations with an isotropic spacing of 1 mm within a 78-mm × 24-mm region, extending 43 mm proximal to the bifurcation apex in the CCA and 35 mm distal to the bifurcation apex in the external and internal carotid arteries. Note that a 1-mm sample spacing is appropriate, as the effective spatial resolution of clinical DUS is approximately 1 mm [26]. In order to ensure consistent positioning of the acquisition grid in relation to each flow phantom, registration to the apex of the bifurcation was performed prior to data collection for each experiment. Ten seconds of Doppler audio data were acquired at each collection site and digitized with a sampling rate of 44.1 kHz for offline postprocessing and analysis.

To allow for statistical analysis in the post-stenotic region, additional measurements were performed in a region of interest (ROI) within the distal ICA. The location of the ROI was optimized based on colour-encoded maps of central plane data in all of the phantoms. The ROI was defined as a 6-mm diameter circular grid consisting of 24 points with 1-mm isotropic spacing, located two CCA diameters (16 mm) distal to the bifurcation in the centre of the ICA. Ten independent measurements were performed for each point in the grid, each containing 10 s of audio data collected using the acquisition parameters described above.

Data analysis

Data analysis of each spectrum consisted of a 1,024-point fast Fourier transform (FFT) with a 1,024-point Hanning window and 50% overlap between consecutive windows, producing an instantaneous Doppler spectrum every 12 ms with a velocity resolution of 1.3 cm·s^{-1}. Each of the resulting 85 velocity power spectra calculated from each

second of data were used to determine mean velocity (v_{mean}), peak velocity (v_{peak}), and spectral width [26]. To characterize the spread associated with the velocity spectrum, spectral width was determined from the full width at half maximum of the velocity spectrum, and the spectral broadening index was calculated as $1 - v_{mean}/v_{peak}$. Several derived parameters were calculated from the periodic ensemble average of ten complete cardiac cycles, including: TI; standard deviation in peak velocities (SDPV); and ensemble-averaged mean velocity ($\overline{v}_{mean}$), peak velocity ($\overline{v}_{peak}$), spectral width (SW), and spectral broadening index (SBI) [26]. The absolute TI was calculated as the RMS deviation in v_{mean} about $\overline{v}_{mean}$, while SDPV was defined as the standard deviation in v_{peak} about $\overline{v}_{peak}$.

Two-dimensional (2D) velocity parameter maps were rendered for each of the 79 time points in the cardiac cycle. To visualize differences in DUS-measured spectral velocity parameters between the non-ulcerated phantom and an ulcerated phantom, the corresponding 2D velocity parameter maps were compared using site-by-site subtraction maps. An intensity-based threshold filter was applied to remove data points collected from outside the lumen.

Statistical analysis

For each of the 79 time points in the cardiac cycle, statistical tests were performed on each DUS parameter, using the mean of ten repetitions (each calculated from the gated ensemble of ten cardiac cycles) at each of the acquisition points in the ROI (n=24). Paired t-tests were performed to test for differences between two models. For quantitative comparisons between models at a specific time point, mean values and corresponding standard errors calculated from ten repetitions at each of 24 points in the ROI (n=240) are reported. The maximum mean value (and corresponding time point) was determined from the mean TI (n=240) at each of the 79 time points, and defined as the maximum TI for the model. Repeated measures one-way analysis of variance (ANOVA) was used to test for the effects of shape and size of ulceration. Each ANOVA was performed on mean values of TI (n=240) for 79 time points in the cardiac cycle (n=79).

Results

Verification of phantom geometry

Visual inspection of the lumen boundary of each phantom determined from micro-CT images demonstrated that a smoothly machined surface was achieved throughout the lumen. The average RMS error in dimensions was 0.15 mm, based on ten measurements of lumen dimension from locations both within the vessel and the ulcer of each phantom. This indicated that the direct-fabrication technique was able to reproduce the prescribed vessel geometries with high fidelity.

Turbulence intensity (TI)

Increased TI was observed in the distal ICA downstream from the site of ulceration. This is indicated in Fig. 2 for the hemispherical ulcer models, where the differences in TI between the ulcerated and non-ulcerated models are visually evident in the corresponding subtraction maps (Fig. 2 C, E, G). The region of elevated TI was located approximately two CCA diameters (16 mm) distal to the apex of the bifurcation, with an extent of approximately one CCA diameter (8 mm). The elevation of TI was most pronounced between 12 ms preceding peak systole and 60 ms following peak systole, as shown in Figs. 3 and 4. During this window around peak systole, the TI measured in the distal ROI (located at an axial distance of 55–60 mm in Fig. 2) was persistently higher in all of the ulcer phantoms than during any phase of the cardiac cycle in the non-ulcerated phantom. The maximum TI (n=240) measured in the distal ROI with corresponding standard error and the time point of occurrence are listed in Table 1. The time of maximum TI occurred between 12 and 36 ms post peak systole in each phantom. The 2-mm hemispherical ulcer phantom exhibited the smallest maximum differences in TI of 6.2±0.7 $cm{\cdot}s^{-1}$ relative to the non-ulcerated model, whereas the largest maximum difference of 10.3±0.7 $cm{\cdot}s^{-1}$ was observed in the ulcer phantom with the distally pointing ellipsoid. Statistically significant differences in TI (95% confidence) were found between the non-ulcerated phantom and each of the ulcerated phantoms. At the time point in the cardiac cycle where the maximum value of TI was measured in the ROI, there was a significant difference in TI in each of the ulcerated phantoms compared to the non-ulcerated phantom with P values of <0.001, as shown in Table 1. Two time intervals in the cardiac cycle during which TI did not exhibit significant differences between all ulcer models and the non-ulcerated model were observed. These occurred at 140–190 ms (i.e. 20–70 ms preceding peak systole) and 430–700 ms (i.e. 220–490 ms following peak systole), corresponding to the two major acceleration phases of the cardiac cycle where downswings in TI were observed. Significant elevations in TI were found in the ulcerated models compared with the non-ulcerated model for all other phases of the cardiac cycle, including during the deceleration phase following peak systole and during diastole when the ulcerated models exhibited a heightened level of steady-state TI. The level of TI measured in the laminar flow region near the CCA midline of the models was 2.2±0.5 $cm{\cdot}s^{-1}$ (mean ± standard deviation) and was not significantly different between models (P=0.87).

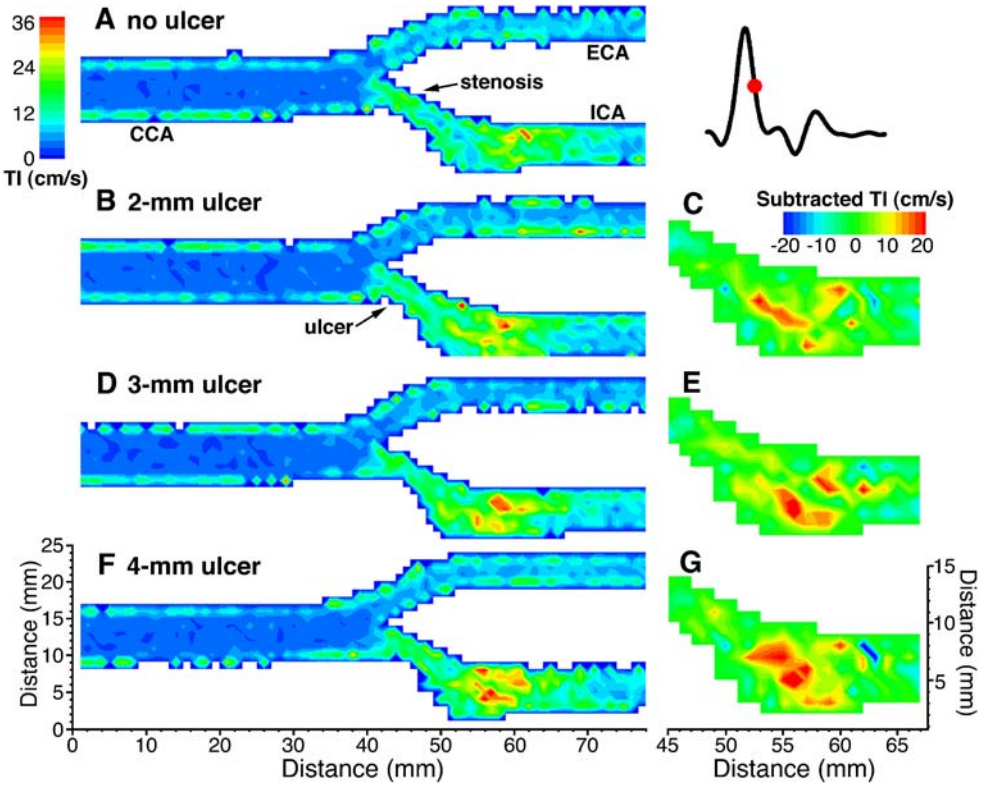

Fig. 2 Colour-encoded maps of TI in the central plane of (**A**) the non-ulcerated phantom and (**B**, **C**) the 2-mm, (**D**, **E**) 3-mm and (**F**, **G**) 4-mm hemispherical ulcer phantoms, at 48 ms post peak systole, where (**C**, **E**, **G**) are subtraction maps of TI in the ICA of the ulcer phantom relative to the non-ulcerated phantom

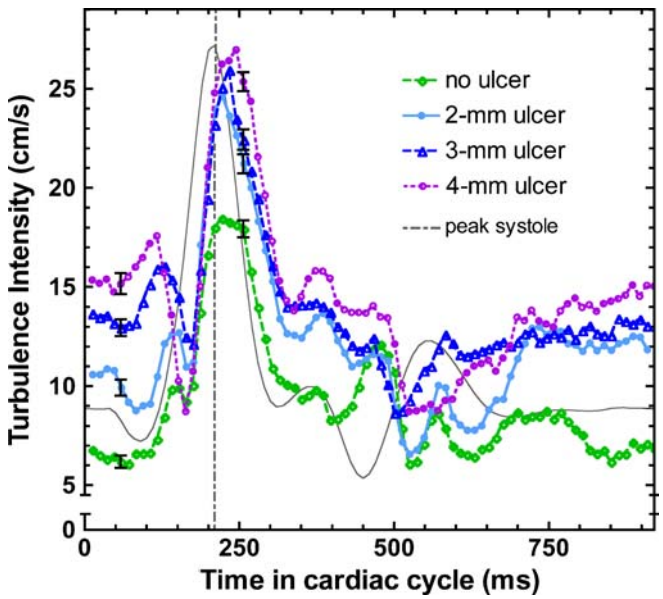

Fig. 3 TI versus cardiac cycle time in the ROI for the non-ulcerated phantom, and the 2-mm, 3-mm and 4-mm hemispherical ulcer phantoms. The value of TI at each time point is an average of ten repetitions (each of ten cardiac cycles) at each of the 24 acquisition sites in the ROI (n=240). Standard errors are shown for two time points: in end diastole (seen at a time of 60 ms) and at 48 ms post peak systole (seen at a time of 264 ms). A schematic of the cardiac waveform is overlaid (*solid grey line*) to indicate the relative positions of systole and diastole. Peak systole occurs at approximately 210 ms, as indicated by the *vertical dashed line*

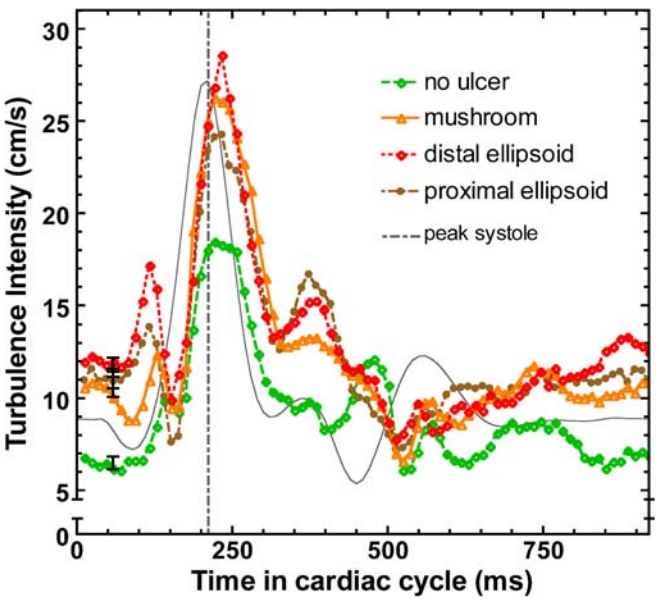

Fig. 4 TI versus cardiac cycle time in the ROI for ulcer phantoms of various shapes (mushroom, ellipsoidal pointing distally and ellipsoidal pointing proximally) and for the non-ulcerated phantom. Standard errors are shown in end diastole (seen at a time of 60 ms). A schematic of the cardiac waveform is overlaid (*solid grey line*) to indicate the relative positions of systole and diastole. Peak systole occurs at approximately 210 ms

Table 1 Maximum TI in the ROI located within the distal ICA

Ulcer geometry	TI ($cm \cdot s^{-1}$)[a]	P[b]	Time post peak systole (ms)
No ulcer	18.5±0.4		12
2-mm hemisphere	24.6±0.6	<0.001	12
3-mm hemisphere	25.9±0.7	<0.001	24
4-mm hemisphere	27.0±0.5	<0.001	36
Mushroom	26.6±0.6	<0.001	12
Ellipsoid pointing distally	28.6±0.6	<0.001	24
Ellipsoid pointing proximally	24.3±0.5	<0.001	24

[a]Values are maximum mean TI ± standard error (n=240)
[b]P values indicate the significance of the differences in means of TI in the ROI (n=24) between the non-ulcerated and ulcerated models at the indicated phase in the cardiac cycle

TI: Effect of ulcer size and shape

TI in the post-stenotic region increased as the diameter of the hemispherical ulcer was increased from 2 mm to 4 mm, as indicated in Figs. 2, 3 and Table 1. One measure of the effect of ulcer size is maximum TI measured in the ROI in the distal ICA, which increased 1.3 $cm \cdot s^{-1}$ between the 2- and 3-mm diameter ulcer and 1.1 $cm \cdot s^{-1}$ between the 3- and 4-mm diameter ulcer. Maximum TI presented at a later time point in the cardiac cycle with increasing diameter of hemispherical ulceration, shifting from 12 ms to 36 ms post peak systole between the 2-mm and 4-mm diameter hemispherical ulcer phantoms. Diastolic values of TI also increased with ulcer size, as shown in Fig. 3. In addition, the spatial extent of elevated TI increased with the diameter of ulceration, although the region of elevation was consistently located at approximately two CCA diameters distal to the bifurcation apex (Fig. 2). A statistically significant effect of ulcer size was observed (P<0.001), as determined by a repeated measures one-way ANOVA of TI in the ROI at 79 time points in the cardiac cycle. A Tukey post-hoc test showed that TI increased as the diameter of ulceration increased (3 mm > 2 mm, and 4 mm > 3 mm, with P<0.001).

A statistically significant effect of ulcer shape (P<0.001) was also indicated by a repeated measures one-way ANOVA of TI in the ROI at 79 points in the cardiac cycle. The ellipsoidal ulcer models with opposite orientations with respect to the direction of blood-flow (distal vs proximal), displayed significantly different levels of TI at 24 ms post peak systole (P<0.001), where TI was 4.3± 0.8 $cm \cdot s^{-1}$ higher downstream from the Type III (distally pointing) ellipsoidal ulcer (Table 1).

Other velocity parameters

As indicated by the mean and peak velocity maps of the longitudinal central plane shown in Fig. 5, the major flow features characteristic of a carotid bifurcation of 50% eccentric stenosis were observed in each of the flow

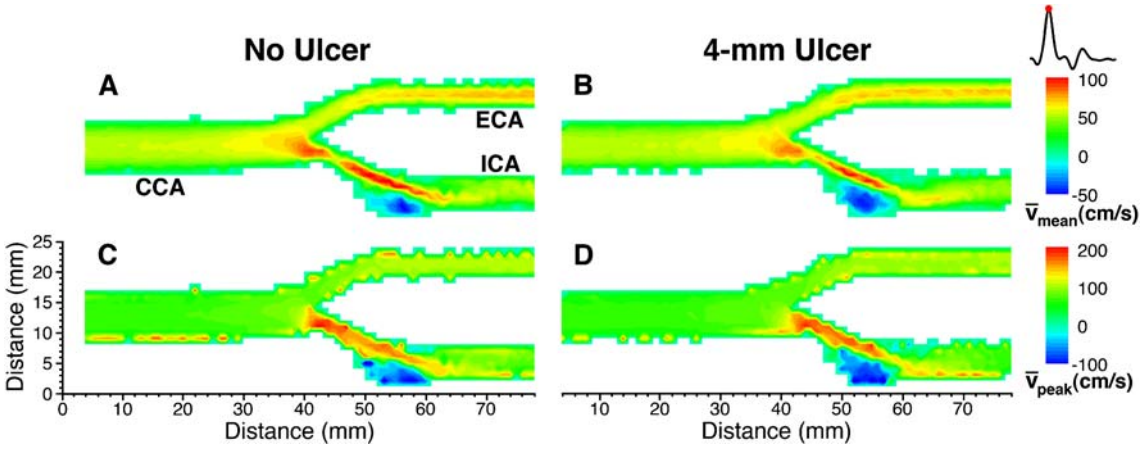

Fig. 5 Colour-encoded maps of ensemble-averaged (**A**, **B**) mean velocity and (**C**, **D**) peak velocity in the central plane of the non-ulcerated phantom (*left column*) and the 4-mm hemispherical ulcer phantom (*right column*) at peak systole

phantoms, including the high-velocity jet through the stenosis and the recirculation zone along the non-flow divider wall of the distal ICA. Peak systolic velocities of approximately 110 cm·s^{-1} (mean) and 180 cm·s^{-1} (peak) corresponding to a 50% (NASCET) stenosis [1], were found in the jet of the stenosis in both non-ulcerated and ulcerated models. The recirculation zone appears near peak systole and persists for 200 ms through the deceleration phase following peak systole. The zone of recirculating flow then reappears to a lesser extent during the smaller deceleration phases of end systole and following the dicrotic notch during diastole.

A comparison of other spectral indices (spectral width, spectral broadening index and standard deviation in peak velocity) in the central plane of the non-ulcerated and 4-mm ulcer phantoms at 48 ms post peak systole are shown in Fig. 6. No distinct differences in SW, SBI or SDPV were observed during the systolic phase of the cardiac cycle as a result of ulceration. This is further demonstrated in Fig. 7, which shows the time course of these additional spectral parameters over the cardiac cycle in the distal ROI. Moderate differences in the values of SW, SBI and SDPV were observed in the ROI for a period of approximately 300 ms during the end of the diastole phase, which roughly coincides with the interval in diastole for which differences in TI were observed.

Discussion

We have shown that the presence of ulceration within a carotid stenosis leads to a significant increase in TI in the distal ICA, as measured by clinical DUS. Offline analysis of velocity spectra, acquired over ten cardiac cycles, indicated regions of elevated TI approximately two CCA diameters (16 mm) distal to the stenosis that peaked between 12–36 ms post peak systole, as shown in Figs. 3 and 4, but remained higher than maximum TI values in the non-ulcerated model for more than 60 ms. In the case of the 4-mm hemispherical ulcer, the severe elevation in TI near peak systole endures for almost 100 ms, which may indicate a window for the detection of ulcers in a clinical setting. While TI is elevated throughout a majority of the cardiac cycle in each of the ulcer models, we believe that the sharp increase immediately following peak systole is of diagnostic value.

From our study of three hemispherical ulcer models, we observed an effect of ulcer dimension on TI, as might be expected. With increasing ulcer diameter, both the area of elevated TI and the absolute TI increased (Figs. 2, 3). While overall ulcer size may be important, the mushroom-shaped ulcer in this study, which had a neck diameter of 2.14 mm, produced distal TI values intermediate to that of the 3- and 4-mm diameter hemispherical ulcers, even though it had a total cavity volume equivalent to the 4-mm diameter hemispherical ulcer. Inlet size, therefore, may be a determinant factor, although the volume of the ulcer cavity may affect the aggregation of platelets and other thrombogenic particles by influencing the degree of circulating flow within the ulcer. In contrast, two ellipsoidal ulcers with identical cavity volumes and neck diameters but opposite orientation with respect to the adjacent bulk flow in the stenosis, produced TI values that differed by as much as

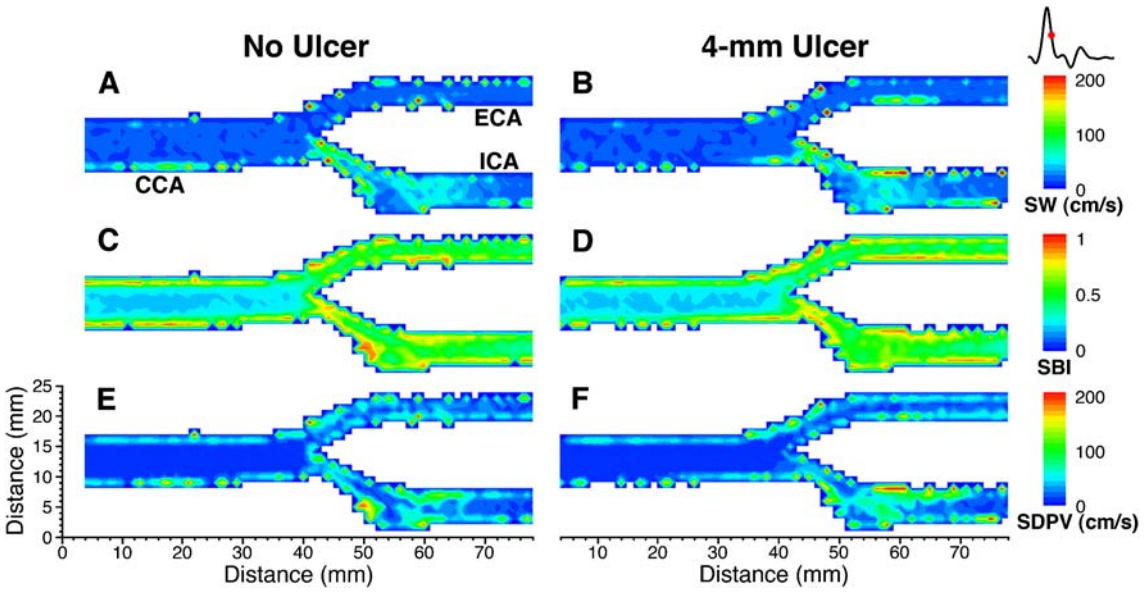

Fig. 6 Colour-encoded maps of ensemble-averaged (**A**, **B**) spectral width, (**C**, **D**) spectral broadening index, and (**E**, **F**) standard deviation in peak velocity in the central plane of the non-ulcerated phantom (*left column*) and the 4-mm hemispherical ulcer phantom (*right column*) at 48 ms post peak systole

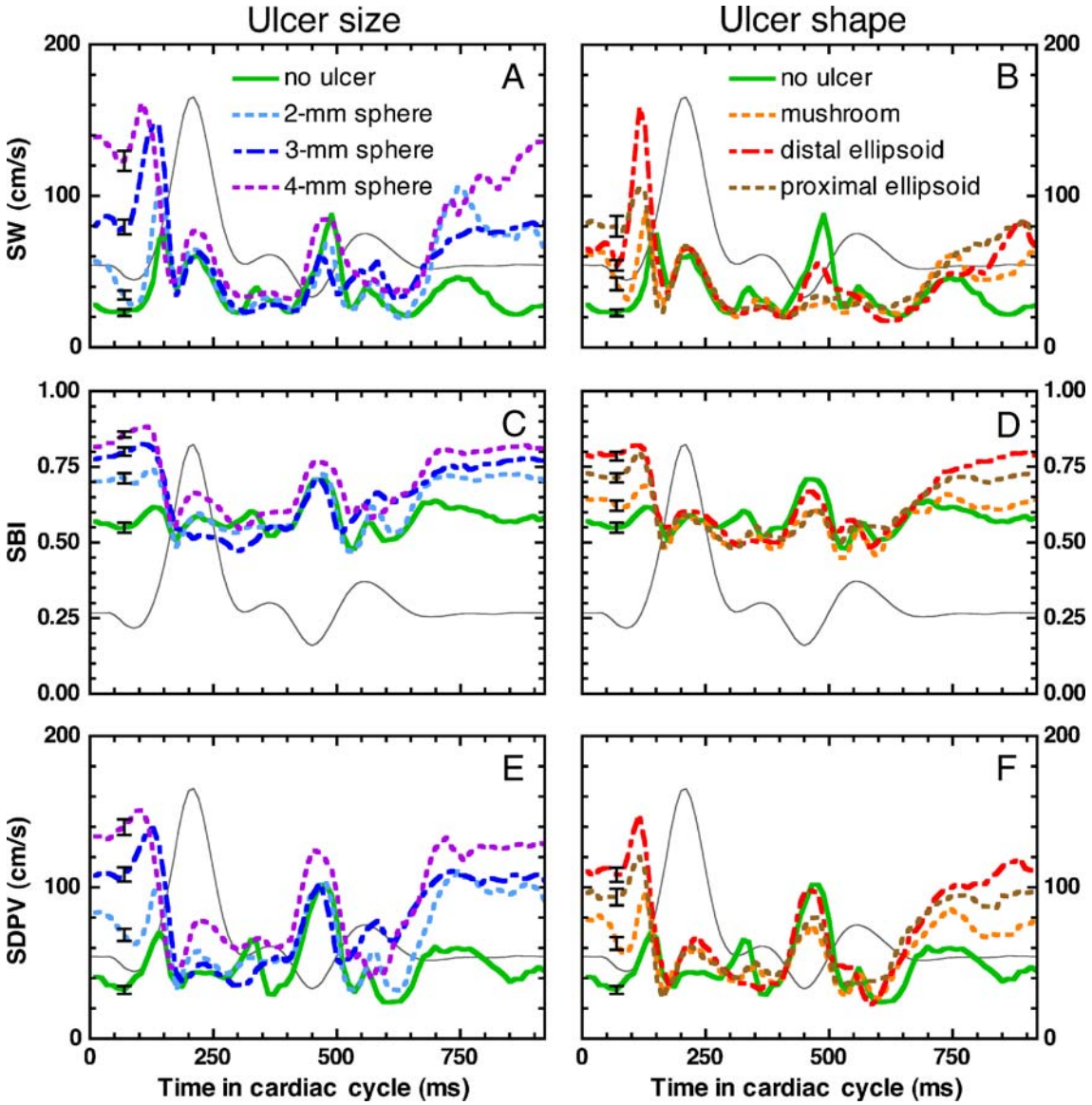

Fig. 7 The DUS parameters (**A**, **B**) spectral width, (**C**, **D**) spectral broadening index, and (**E**, **F**) standard deviation in peak velocity versus cardiac cycle time in the ROI, where a comparison with ulcer size is shown in the *left column* (2-mm, 3-mm and 4-mm hemispherical ulcers) and a comparison with ulcer shape is shown in the *right column* (mushroom, ellipsoidal pointing distally and ellipsoidal pointing proximally). Schematics of the cardiac waveform are overlaid on each graph (*solid grey line*) to indicate the relative positions of systole and diastole. Peak systole occurs at approximately 210 ms. Standard errors are shown for a representative time point of 60 ms

4.3±0.1 cm·s^{-1}. Ulcers with either a larger inlet area or a more accessible configuration may permit greater flow entry into the ulcer cavity during diastole, when acceleration at the stenosis is low, and a greater degree of exiting flow into the high-velocity jet during peak systole [9]. All of these factors of ulcer morphology are likely to influence the flow entering, circulating, and exiting the ulcer.

We also investigated additional parameters that can provide an indication of flow disturbances. In contrast to TI, the Doppler parameters spectral width, spectral broadening index and standard deviation in peak velocity were not sensitive indicators of carotid ulcerated lesion surface, exhibiting little or no significant difference during the dynamic phases of the cardiac cycle with varying condition of ulceration. While not providing a clear diagnostic window, these parameters did display a stratification of values based on ulcer size and shape for approximately 300 ms during the diastolic phase of the cardiac cycle, when the pulsatile response is diminished and steady-state levels are more apparent (Fig. 7). This stratification effect is also observed with TI during the same time period (Figs. 3, 4), and suggests that spectral data extracted from

diastolic measurements may provide some information to aid in the classification of ulcer size and shape. It should be noted, however, that conventional clinical DUS is susceptible to large errors in estimations of peak velocities and spectral width [17, 31]. TI, on the other hand, is a truer representation of velocity variance within the flow field, since it is based on mean velocities calculated from the first moment of the average velocity spectrum [16]. Consequently, it is also relatively immune to intrinsic spectral broadening, which has a symmetric effect on the shape of the Doppler spectrum [17]. For these reasons, TI is a more robust and appropriate diagnostic indicator for the assessment of flow disturbances associated with the ulcerated carotid lesion.

Our results agree with previous studies, which have shown that the introduction of ulceration in a stenosed carotid bifurcation produces observable flow disturbances, using numerical simulation [8] and experimental slipstream visualization techniques [9]. While Lesniak et al. [32] have previously investigated Doppler techniques (using a laser Doppler anemometer and a pulsed Doppler flowmeter) to observe alterations in blood-velocity patterns due to surface irregularities in the carotid artery vessel, our approach differed in that surface irregularity in the current study was modelled as physiologically realistic ulcerations, as opposed to simple protrusions on the vessel wall surface. In addition, our precise control of ulcer shape and size allowed us to investigate the effect of ulcer geometry rather than simply introducing a higher frequency of protrusion. Our use of a conventional clinical DUS system combined with offline analysis is also more amenable to future applications in a clinical setting.

While the rigidity of the phantoms used in this study enabled desired vessel geometries with small well-defined features to be reproduced accurately and faithfully, the associated compromise is that they did not model the effects of vessel compliance observed in human vasculature. However, it has been shown that there is a tendency for vessel wall motion to decrease considerably with age and disease [33], where vessels in an elderly population exhibit a distension of only 5%, as opposed to 12–14% change in vessel diameter in a young population [34]. Computational flow simulations [35] and fluid dynamics derivations [36] have demonstrated that this small degree of vessel compliance has little effect on the global characteristics of flow behaviour in the carotid stenosis. Furthermore, by employing matched model geometries for this study, where all parameters are maintained except for the plaque morphology at the level of the apex on the non-flow divider wall, the effects of ulceration can be isolated.

Due to the sample volume limitations of medical DUS, our described technique does not enable the characterization of flow within the ulcer or distinction between turbulence and coherent disturbances in the downstream flow field. However, the use of a clinical diagnostic system makes our measurements in the distal ICA more representative of clinically available data. Further studies in basic research, using experimental techniques [e.g. particle imaging velocimetry (PIV)] or numerical methods [e.g. computational fluid dynamics (CFD)], could be used to improve the understanding of flow within the ulcer and the initiation of flow disturbances downstream. They may also elucidate the involvement of these hemodynamic factors in the underlying thrombogenic process [37]. Note that because vessel lumen geometries can be non-invasively extracted from the phantoms with high fidelity using high-resolution micro-CT, the same geometries can be used to create transparent optical phantoms for study using PIV, and for CFD models. Fundamental research—combined with advancements in clinical techniques—will lead to a greater understanding of ulcer plaque conditions and, thereby, more accurate patient assessment and management.

We have reported an effect of ulceration in the development of post-stenotic flow disturbances in the carotid bifurcation, indicating that it may be beneficial to evaluate the DUS measurement of TI as a potential diagnostic indicator of plaque surface roughness. A measure of plaque irregularity using DUS may complement the evaluation of percent stenosis in assessing the risk of carotid artery-related stroke, particularly for moderate grade stenoses. The detection of ulcers in moderate stenoses, such as demonstrated in this study, is of importance for the identification of patients who are not currently indicated for carotid endarterectomy based solely on stenosis severity, but may in fact benefit from surgical therapy due to their higher risk of stroke. The clinical assessment of TI could be easily integrated as an adjunct to the current conventional DUS examination using peak systolic velocity, with little interruption to the clinical workflow. Since calculations of TI are performed using offline analysis, the examination procedure would simply require a modification to collect data from multiple cardiac cycles. In addition, this method of using measures of TI for ulcerated plaque detection has the potential to be implemented using alternate techniques that have the capability to temporally resolve and quantify velocity fluctuations, such as with phase-contrast magnetic resonance imaging (MRI) [38]. Nevertheless, we would like to caution that although we found statistically significant increases in TI due to the effect of ulceration, the absolute increase in TI was moderate (i.e. 6–10 $cm{\cdot}s^{-1}$). By controlling for parameters of flow and stenosis geometry, our in-vitro set-up was designed to detect such differences in downstream TI. However, it will certainly be more difficult to discriminate between diseased carotid vessels with and without ulceration in-vivo, due to the natural inter-patient variation in vascular geometry [39] and hemodynamic conditions [29, 40], as well as greater measurement uncertainties in the clinical environment. If ulcer detection beyond a moderate stenosis grade is desired, it may be important to determine the co-relation of stenosis severity and ulceration to distal TI, as TI is also

expected to increase with stenosis grade [26]. It is also possible that elevated levels of TI will be a useful indication of overall risk, regardless of the source. Apart from identifying a parameter of potential diagnostic utility, our observation of exacerbated levels of disturbed flow downstream from ulceration has the parallel implication that distal hemodynamics may play a role in the process of thrombogenesis. Our findings support other studies that implicate both hemodynamic and biochemical factors in ischemic stroke.

Conclusion

In-vitro flow experiments facilitated a direct comparison of Doppler velocity data and derived blood-flow parameters between ulcerated and non-ulcerated plaque geometries in the stenosed carotid bifurcation. We have demonstrated that clinical DUS is able to detect modifications of the distal flow field produced by ulceration in the carotid lesion, using the velocity-based parameter TI.

Acknowledgement The authors would like to acknowledge ATL (Advanced Technology Laboratories, Philips, Seattle, USA) for the UM9 ultrasound unit. Financial support has been provided by the Heart and Stroke Foundation of Ontario (grant #T-6427). Vessel models were fabricated with support from the Canadian Institutes of Health Research (operating grant #MOP-77964). Dr. Holdsworth is the Dr. Sandy Kirkley Chair of Musculoskeletal Research in the Schulich School of Medicine and Dentistry. Dr. Poepping is supported by a University Faculty Award from the Natural Sciences and Engineering Research Council of Canada. E. Y. Wong is supported by a Canadian Institutes of Health Research Frederick Banting and Charles Best Canada Graduate Scholarships Doctoral Award.

References

1. Grant EG, Benson CB, Moneta GL et al (2003) Carotid artery stenosis: grayscale and Doppler ultrasound diagnosis—Society of Radiologists in Ultrasound consensus conference. Ultrasound Q 19:190–198
2. Wardlaw JM, Chappell FM, Best JJ et al (2006) Non-invasive imaging compared with intra-arterial angiography in the diagnosis of symptomatic carotid stenosis: a meta-analysis. Lancet 367:1503–1512
3. Hankey GJ (1999) Stroke prediction and prevention by carotid endarterectomy: keep an eye on the doughnut and not just the hole. Cerebrovasc Dis 9:345–350
4. Eliasziw M, Streifler JY, Fox AJ et al (1994) Significance of plaque ulceration in symptomatic patients with high-grade carotid stenosis. North American Symptomatic Carotid Endarterectomy Trial. Stroke 25:304–308
5. Sitzer M, Muller W, Siebler M et al (1995) Plaque ulceration and lumen thrombus are the main sources of cerebral microemboli in high-grade internal carotid artery stenosis. Stroke 26:1231–1233
6. Orlandi G, Parenti G, Landucci Pellegrini L et al (1999) Plaque surface and microembolic signals in moderate carotid stenosis. Ital J Neurol Sci 20:179–182
7. Motomiya M, Karino T (1984) Flow patterns in the human carotid artery bifurcation. Stroke 15:50–56
8. Birchall D, Zaman A, Hacker J et al (2006) Analysis of haemodynamic disturbance in the atherosclerotic carotid artery using computational fluid dynamics. Eur Radiol 16:1074–1083
9. Imbesi SG, Kerber CW (1998) Why do ulcerated atherosclerotic carotid artery plaques embolize? A flow dynamics study. AJNR Am J Neuroradiol 19:761–766
10. Mustard JF, Murphy EA, Rowsell HC et al (1962) Factors influencing thrombus formation in vivo. Am J Med 33:621–647
11. Sakariassen KS, Holme PA, Orvim U et al (1998) Shear-induced platelet activation and platelet microparticle formation in native human blood. Thromb Res 92:S33–S41
12. Stein PD, Sabbah HN (1974) Measured turbulence and its effect on thrombus formation. Circ Res 35:608–614
13. Hoeks AP, Hennerici M, Reneman RS (1991) Spectral composition of Doppler signals. Ultrasound Med Biol 17:751–760
14. Sigel B, Gibson RJ, Amatneek KV et al (1970) A Doppler ultrasound method for distinguishing laminar from turbulent flow. A preliminary report. J Surg Res 10:221–224
15. Garbini JL, Forster FK, Jorgensen JE (1982) Measurement of fluid turbulence based on pulsed ultrasound techniques. Part 2. Experimental investigation. J Fluid Mech 118:471–505
16. Dunmire B, Pagel G, Beach KW et al (2001) Post stenotic flow disturbances in a steady flow model. In: SPIE-Int Soc Opt Eng, San Diego, pp 502–513
17. Evans DH, McDicken WN (2000) Doppler ultrasound: physics, instrumentation and signal processing. Wiley, Chichester
18. Wong EY, Thorne ML, Nikolov HN et al (2008) Doppler ultrasound compatible plastic material for use in rigid flow models. Ultrasound Med Biol 34:1846–1856
19. Smith RF, Rutt BK, Fox AJ et al (1996) Geometric characterization of stenosed human carotid arteries. Acad Radiol 3:898–911
20. Fox AJ (1993) How to measure carotid stenosis. Radiology 186:316–318
21. Lovett JK, Gallagher PJ, Hands LJ et al (2004) Histological correlates of carotid plaque surface morphology on lumen contrast imaging. Circulation 110:2190–2197
22. Lovett JK, Rothwell PM (2003) Site of carotid plaque ulceration in relation to direction of blood flow: an angiographic and pathological study. Cerebrovasc Dis 16:369–375
23. Troyer A, Saloner D, Pan XM et al (2002) Major carotid plaque surface irregularities correlate with neurologic symptoms. J Vasc Surg 35:741–747
24. Saba L, Caddeo G, Sanfilippo R et al (2007) CT and ultrasound in the study of ulcerated carotid plaque compared with surgical results: potentialities and advantages of multidetector row CT angiography. AJNR Am J Neuroradiol 28:1061–1066

25. Rothwell PM, Gibson R, Warlow CP (2000) Interrelation between plaque surface morphology and degree of stenosis on carotid angiograms and the risk of ischemic stroke in patients with symptomatic carotid stenosis. On behalf of the European Carotid Surgery Trialists' Collaborative Group. Stroke 31:615–621
26. Poepping TL, Nikolov HN, Rankin RN et al (2002) An in vitro system for Doppler ultrasound flow studies in the stenosed carotid artery bifurcation. Ultrasound Med Biol 28:495–506
27. Ramnarine KV, Nassiri DK, Hoskins PR et al (1998) Validation of a new blood-mimicking fluid for use in Doppler flow test objects. Ultrasound Med Biol 24:451–459
28. Thorne ML, Poepping TL, Rankin RN et al (2008) Use of an ultrasound blood-mimicking fluid for Doppler investigations of turbulence in vitro. Ultrasound Med Biol 34:1163–1173
29. Holdsworth DW, Norley CJ, Frayne R et al (1999) Characterization of common carotid artery blood-flow waveforms in normal human subjects. Physiol Meas 20:219–240
30. Frayne R, Holdsworth DW, Gowman LM et al (1992) Computer-controlled flow simulator for MR flow studies. J Magn Reson Imaging 2:605–612
31. Hoskins PR (1999) A review of the measurement of blood velocity and related quantities using Doppler ultrasound. Proc Inst Mech Eng [H], J Eng Med 213:391–400
32. Lesniak B, Kaluzynski K, Liepsch D et al (2002) The discrimination of stenosed carotid bifurcation models with smooth and irregular plaque surface. Part I. Laser and ultrasonic Doppler flow studies. Med Eng Phys 24:309–318
33. Benetos A, Waeber B, Izzo J et al (2002) Influence of age, risk factors, and cardiovascular and renal disease on arterial stiffness: clinical applications. Am J Hypertens 15:1101–1108
34. Hansen F, Mangell P, Sonesson B et al (1995) Diameter and compliance in the human common carotid artery—variations with age and sex. Ultrasound Med Biol 21:1–9
35. Perktold K, Rappitsch G (1995) Computer simulation of local blood flow and vessel mechanics in a compliant carotid artery bifurcation model. J Biomech 28:845–856
36. Dewey CF (1979) Fluid mechanics of arterial flow. In: Wolf W, Werthessen NT (eds) Dynamics of arterial flow. Adv Exp Med Biol 115:55–103
37. Raz S, Einav S, Alemu Y et al (2007) DPIV prediction of flow induced platelet activation—comparison to numerical predictions. Ann Biomed Eng 35:493–504
38. Dyverfeldt P, Sigfridsson A, Kvitting JP et al (2006) Quantification of intravoxel velocity standard deviation and turbulence intensity by generalizing phase-contrast MRI. Magn Reson Med 56:850–858
39. Schulz UG, Rothwell PM (2001) Major variation in carotid bifurcation anatomy: a possible risk factor for plaque development? Stroke 32:2522–2529
40. Younis HF, Kaazempur-Mofrad MR, Chan RC et al (2004) Hemodynamics and wall mechanics in human carotid bifurcation and its consequences for atherogenesis: investigation of inter-individual variation. Biomech Model Mechanobiol 3:17–32